
Head-to-head comparison of the penetration efficiency of lipid-based nanoparticles in a 3D tumor spheroid model

Maria Niora,^a Dennis Pedersbæk,^b Rasmus Münter,^b Matilda Felicia de Val Weywadt,^b Thomas Lars Andresen,^b Jens Bæk Simonsen^{b*} and Liselotte Jauffred^{a*}

^a The Niels Bohr Institute, University of Copenhagen, Blegdamsvej 17, Denmark. ^b DTU Health Tech, Technical University of Denmark, Kongens Lyngby, Denmark; E-mail: jbak@dtu.dk, jauffred@nbi.dk.

Most tumor-targeted drug delivery systems must overcome a large variety of physiological barriers before reaching the tumor site and diffuse through the tight network of tumor cells. Many studies focus on optimizing the first part, the accumulation of drug carriers at the tumor site, ignoring the penetration efficiency, i.e., a measure of the ability of a drug delivery system to overcome tumor surface adherence and uptake. We used 3D tumor spheroids in combination with light-sheet fluorescence microscopy in a head-to-head comparison of a variety of commonly used lipid-based nanoparticles, including liposomes, PEGylated liposomes, lipoplexes and reconstituted high-density lipoproteins (rHDL). Whilst PEGylation of liposomes only had minor effects on the penetration efficiency, we show that lipoplexes mainly associated to the periphery of tumor spheroids, possibly due to their positive surface charge leading to fusion with the cells at the spheroid surface or aggregation. Surprisingly, the rHDL showed significantly higher penetration efficiency and high accumulation inside the spheroid. While these findings indeed could be relevant when designing novel drug delivery systems based on lipid-based nanoparticles, we stress that the used platform and detailed image analysis is a versatile tool for *in vitro* studies of the penetration efficiency of nanoparticles in tumors.

Keywords: drug delivery, tumor spheroids, light-sheet microscopy, penetration efficiency, reconstituted high-density lipoprotein, liposomes, lipoplexes

Introduction

Nanoparticles (NPs) have over the last decades been established as promising drug carriers for cancer therapy^{1–3}. The advantages of using NPs as drug carriers, includes specific targeting and enhanced drug stability and accumulation in tumor tissue relative to free drugs^{4,5}. Especially lipid-based NPs are attractive due to their high bio-compatibility compared to other nanosized drug carriers, e.g., gold NPs or quantum dots^{2,3}. Most often, clinically approved lipid-based drug delivery systems, rely on passive accumulation at the tumor site^{3,4,6}.

The majority of studies on NP drug delivery focus on the accumulation of NPs in the tumor tissue (through biodistribution studies), and are less concerned with the penetration profile of the NPs into the tumor. We emphasize that the penetration efficiency of the NPs is an important parameter as the therapeutic efficiency could be limited when the drug is only delivered to the outermost cells of the tumor^{7,8}. Whilst it is well-established that NP penetration depends on the physicochemical properties of the NPs, e.g. size^{9–12}, a detailed head-to-head comparison of the penetration of a broad selection of lipid-based NPs is still wanted; to learn which kind of lipid-based NPs to use for a certain drug candidate. Hence, this study

provides a comparative investigation of the penetration efficiencies of liposomes (Lip), PEGylated liposomes (PEG-Lip), reconstituted high-density lipoproteins (rHDL) and lipoplexes (LPX), which have all reached clinical trials^{2,13,14}. As non-lipid control we used polystyrene nanoparticles (PNP) (Fig. 1). Briefly, liposomes (Lip and PEG-Lip) are some of the most commonly used drug carriers. They are spherical vesicles comprised of a lipid bilayer and an aqueous core, while surface grafting of polyethylene glycol (PEG) is frequently used to increase their blood circulation time^{2,15,16}. LPX are complexes of nucleic acids that are stabilized by cationic lipids¹³, and are usually used for gene-targeting applications². The rHDL are biomimetic particles similar to the endogenous high-density lipoproteins (HDL), a natural lipid transporter in the body¹⁴; hence, rHDL are promising drug delivery carriers for various applications¹⁷. There are several variants of the rHDL/HDL-mimicking particles¹⁴, and in this study we used the ~ 10 nm-sized discoidal rHDL consisting of a lipid bilayer stabilized at the edge by two apolipoproteins A-I (apoA-I).

The lipid-based NPs used in here differ in several aspects like i) size, ii) surface charge, iii) surface chemistry and iv) targeting mechanisms. For the latter, only rHDL is believed to be actively targeting as it is recognized by the scavenger receptor class B type 1 (SR-BI) that is over-expressed in many

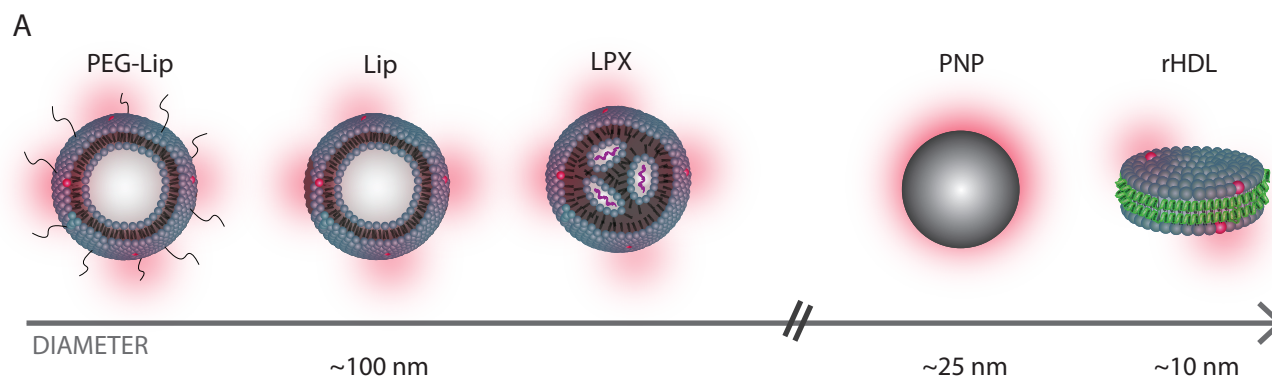


Fig. 1 Overview of the NPs in this study. Sketch of the lipid-based NPs used in this study: PEGylated liposomes (PEG-Lip), liposomes (Lip), lipoplexes (LPX), and reconstituted high-density lipoproteins (rHDL), consisting of lipid bilayers (blue), aqueous cores (white), fluorescent markers (red), nucleic acids (purple), and apoA-I proteins (green). For comparison we also used a non-lipid particle (PNP).

types of cancer cells^{14,18}, including the U87-MG brain cancer cells used in this study¹⁹.

To investigate the NP uptake and penetration, we used an *in vitro* 3D tumor spheroid model^{20,21}, which is a well-established drug screening system^{22–24}. Even though this simple system is grown from monocultures, it still preserves essential features present in cancer tumors *in vivo*; i.e. rapid proliferation at the surface and slow metabolism - or necrosis - in the center of spheroids²⁵. The majority of studies of NP distributions in tumor spheroids use tumor spheroid fixation^{26–34}, often in combination with histological sectioning^{7,35–38}. Nevertheless, there are also reports of NP penetration in live tumor spheroids using confocal-scanning microscopy^{39–49}. Live imaging of NP-treated tumor spheroids ensures that the studied NPs preserve localization, stability, and emission wavelength; as indicated for semi-conducting NPs⁵⁰. However, the high scattering and absorption of live tissue⁵¹ limits imaging depth. Thus, to overcome these constraints we used an Airy beam light-sheet microscope^{52,53} that allows for optical sectioning with little bleaching or photo-damage⁵⁴. With this setup we combine deep imaging of NPs with single-cell resolution of tumor spheroids of hundreds of micrometers^{26,55}.

This study is a head-to-head comparison of penetration efficiencies of several lipid-based NPs commonly used for drug delivery. We use a 3D tumor spheroid model in combination with optical sectioning and a custom-made analysis procedure, and we find that clustering on the tumor spheroid surface and penetration efficiency varies significantly among the tested lipid-based NP types. This *in vitro* platform can easily be adapted to study the penetration of a large variety of fluorescently labeled NPs. Hence, we provide an important tool to screen and optimize the penetration efficiency of NPs, before

conducting more complex *in vivo* studies.

Results and discussion

To study the penetration efficiency of the NPs, we used a brain cancer tumor spheroid model grown from a seed of (~500 cells/well) U87-MG cells in round-bottom ultra-low attachment wells. While negatively charged coating impedes cell attachment to the wells, gravitation assists agglomeration and subsequent spheroid growth (Fig. 2A)^{56,57}. Spheroids were harvested after 3 days, where they had reached a final radius of $134 \pm 10 \mu\text{m}$ (mean \pm SD, N=19). All spheroids were confirmed to attain similar morphological characteristics.

Preparation and characterization of the NPs

The lipid-based NPs (Fig. 1) were prepared using standard methods as described in details elsewhere for liposomes⁵⁸, LPX⁵⁹ and rHDL¹⁸. Briefly, Lip and PEG-Lip were formed by hydration of freeze-dried lipids, followed by extrusion through a 100 nm filter. LPX were prepared by the ethanol-injection technique, where lipids dissolved in ethanol were rapidly injected into aqueous buffer containing the nucleic acid CpG. rHDL were prepared by the detergent depletion method, where lipids were dissolved with detergents that subsequently were depleted using Bio-BeadsTM in the presence of the apolipoprotein A-I (apoA-I), to induce self-assembly of rHDL. The NPs' size and surface charge, i.e. zeta potential, are listed in Table 1.

The distribution and penetration of the lipid-based NPs were studied by detection of the fluorescent label DiI in the NPs. We confirmed that DiI was stably incorporated into the lipid-based NPs (Supplementary Information Fig. S1), as

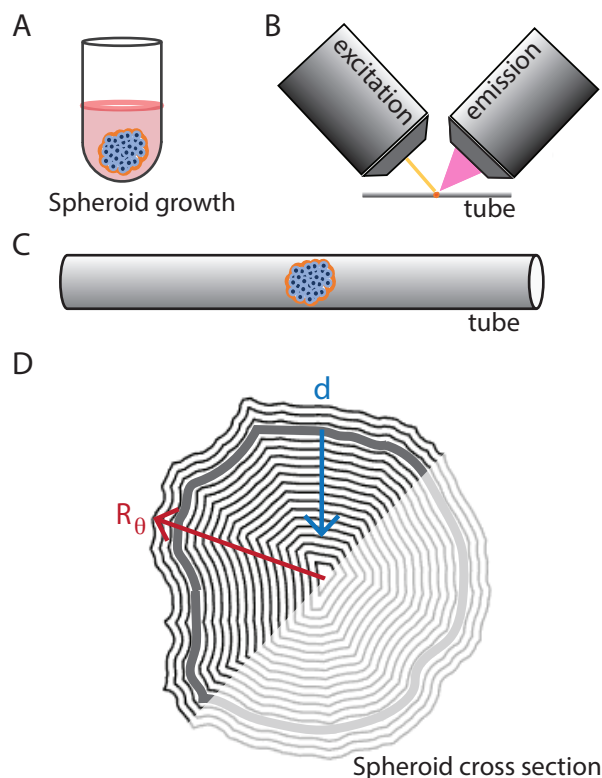


Fig. 2 Overview of the experimental setup. **A:** Illustration of gravitation-assisted tumor spheroid growth. **B:** Sketch of a spheroid mounted for imaging in an Airy beam light-sheet microscope; with an objective for the (yellow) light sheet (excitation) and one for collection of the emitted light (emission). **C:** Close up of the a spheroid mounted in a tube for imaging. **D:** An example of a spheroid cross section mask, where the radial vector from origo to the mask's boundary, R_θ varies in length in respect to the polar angle θ . The mask boundary was slightly larger than the spheroid's surface (grey contour) and the blue vector indicates the tumor depth, d . We restricted our analysis to the half-spheroid closest to the light-sheet objective (excitation).

consistent with previous studies using similar types of fluorophores^{15,18}. We emphasize that all the lipid-based NPs were prepared with equal mol% of fluorophores (0.5% DiI), and that the concentration of the NPs was adjusted such that the amount of fluorophores (based on absorbance) was equal in each sample (Supplementary Information Fig. S2). Thus, we assume that the lipid concentration was the same in each sample. Note that due to the different sizes of the lipid-based NPs, this implies that the NP particle concentration varied between samples.

Distribution of NPs in tumor spheroids

NP-treated tumor spheroids were optically sectioned (Fig. 2B,C) in 400 nm steps to measure fluorescence intensity on planar cross-sections of the spheroids. Notably, the intensity of the nuclear stain gradually decreased towards the center of the spheroids, which is likely explained by the diffusion gradient⁷ and effects from attenuation of the exciting/emitting light at increasing depths⁵⁴. Interestingly, the cross-sections (Fig. 3) show a clear difference in the distribution of the different NPs in the tumor spheroids. While spheroids treated with Lip, PEG-Lip, rHDL, and PNP exhibited fluorescence intensity distributed across the whole cross-section (though with varying intensity), LPX accumulated primarily at the spheroid surface. Areas with augmented fluorescence were observed for rHDL, Lip and LPX, and while these areas were confined to the spheroids' surface for LPX and Lip, they also appeared deeper in the spheroids for rHDL. The augmented fluorescence likely corresponds to either aggregation of particles or high local cellular uptake of NPs. In particular, LPX, due to positive surface charges, might effectively fuse with the outermost cells, or aggregate in the culture medium (at 37 °C), since LPX is considered relatively unstable without PEGylation⁶⁰. Aggregation of LPX would likely render their size larger than the pores in the tumors thereby impeding penetration, while adherence to the surface of the cells or cellular uptake prevents aggregated LPX from being washed out before imaging. Similarly, Lip are considered more prone to aggregation than PEG-Lip^{2,61,62}. However, in contrast to the initially smaller LPX, the neutral surface charge of the Lip possibly allowed them to penetrate deeper into the tumor due to inferior NP-cell interactions, before aggregation or cellular uptake. On the other hand, rHDL showed enhanced accumulation at much greater penetration depths. This could in part be ascribed to the smaller size of rHDL, allowing them to pass more easily through the interstitial space between the cells, like it is the case for PNP.

NP tumor spheroid penetration

The imaging of a dense spheroid is in brief limited by two conditions: i) the attenuation of the fluorescence emission and ii) the attenuation of the exiting laser through the spheroid. To balance (i) we did not use the cross section from the spheroid equator but instead a cross section closer to the imaging objective (emission Fig. 2B) at a depth of 100-140 μm . Therefore, the measured intensities were averaged over 40 μm , which corresponds to 100 frames (Supplementary Information Fig. S3). Furthermore, to redeem the effect of (ii) we restricted our analysis to the half of the cross section closest to the exiting laser (Fig. 2D) and to a maximum depth of 80 μm .

From the masks of the averaged cross sections, we defined the spheroid surface ($d = 0 \mu\text{m}$) as the maximum intensity

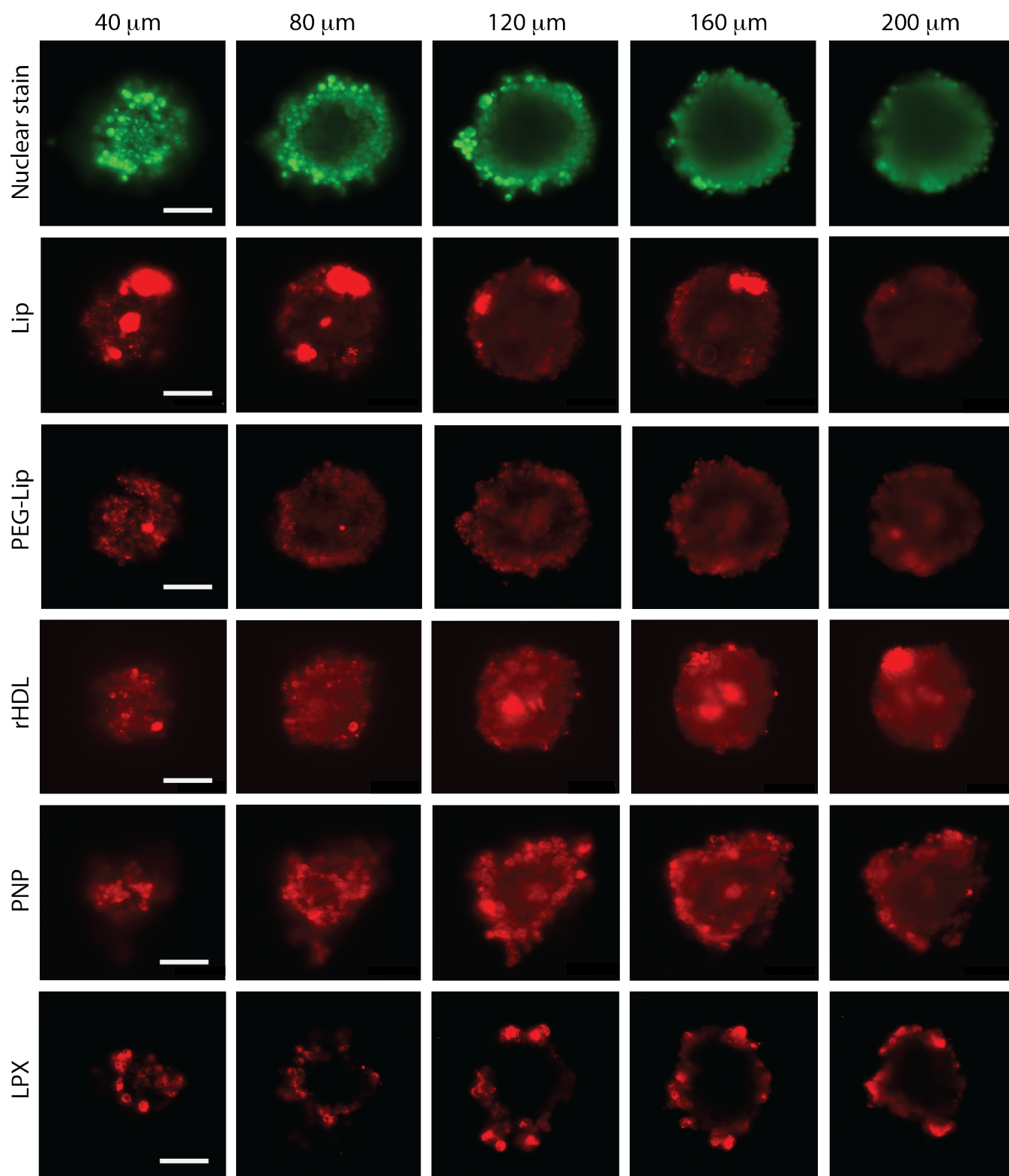


Fig. 3 Cross-sections of U87-MG tumor spheroids treated with NPs. The pseudo-colored and images are representative examples of optical sections from spheroids at different depths in axial direction (40 μm - 200 μm). The spheroids were all nuclear stained (green) and treated with NPs (red): Lip, PEG-Lip, rHDL, PNP, or LPX, for 5 hours. Images have uneven contrast settings between the different NPs, and the scale bars correspond to 100 μm .

	Lip	PEG-Lip	LPX	rHDL	PNP
Size (nm)	114 ± 35.9	112 ± 25.9	77.2 ± 28.7	8.70 ± 1.70	24.1 ± 6.77
Zeta potential (mV)	0.827 ± 6.24	-8.83 ± 9.43	9.96 ± 4.43	-9.39 ± 5.27	-31.0 ± 20.1

Table 1 Characterization of the NPs used in the study. The mean size is based on number [%] from dynamic light scattering measurements. Data represent mean±SD.

depth. As the surface of the spheroid is rough, the radius of the spheroid, R_θ , is changing in respect to the polar angle, θ (Fig. 2D). Therefore, the intensity in a specific depth, d , of the averaged cross section was quantified as follows⁶³:

$$\langle I \rangle = \frac{1}{M} \sum_{i=1}^M I(x_i, y_i), \quad (1)$$

for the M pairs of pixels, (x_i, y_i) , that fulfill the requirement

$$x_i^2 + y_i^2 = (R_\theta - d)^2. \quad (2)$$

We found the normalized intensity profiles $\langle I \rangle$ averaged over all N spheroids of the nuclear stain (grey) and the investigated NPs, as a function of spheroid depth d (Fig. 4). Regardless of the natural variations among the spheroids, the penetration profiles were specific for each type of NPs. Consistent with the cross-section images (Fig. 3), we observed a gradual decrease of the nuclear stain intensity over d . Furthermore, we observed that both rHDL and LPX exhibited high surface adhesion. However LPX remained at the spheroid rim, while all the other NPs penetrated more effectively towards the center of the tumor spheroid.

The penetration depth can be interpreted by the declination of the surface intensity by half, $d_{1/2}$ for the averaged profile. This measure confirmed the limited penetration depth of LPX, $d_{1/2} = 26 \mu\text{m}$, in contrast to the larger penetration depths of Lip, $d_{1/2} = 39 \mu\text{m}$ and PEG-Lip $d_{1/2} = 67 \mu\text{m}$. The larger penetration depth of PEG-Lip relative to Lip could be attributed to reduced interactions with the cells due the PEGylation, thus allowing for increased penetration into the tumor spheroid, as also reported elsewhere for PEGylated NPs⁷. Though the $d_{1/2}$ indeed is a descriptive measure, it is not instrumental for the analysis of penetration profiles that differ from an exponential decay. For instance, rHDL had a unique secondary peak ($d = 80 \mu\text{m}$). Furthermore, PNP did not reduce fluorescence intensity by half at the measured depths, although the intensity gradually decreased after the first surface cell layers.

The up-concentration in depth observed for rHDL might be explained by aggregation. Although rHDL are relatively stable^{64,65}, rHDL aggregation towards the spheroid core might occur due to the slightly more acidic environment (relative to the surface), caused by the increased lactate production from the oxygen-deficient cells⁶⁶, as HDL-associated apoA-I can unfold under acidic conditions⁶⁷. Interestingly, the PNP

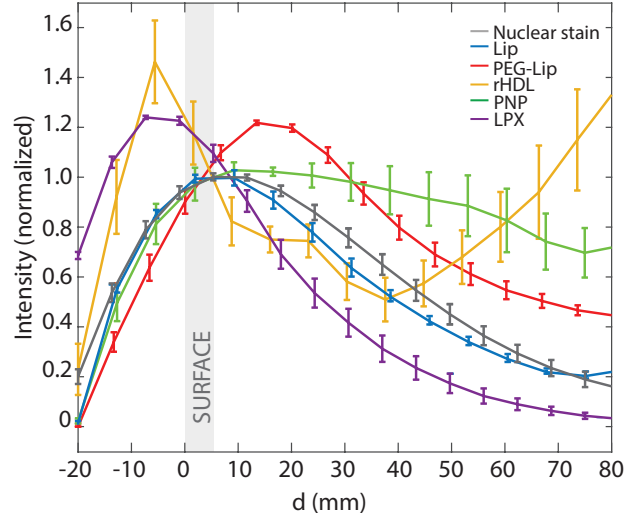


Fig. 4 Penetration of NPs in U87-MG tumor spheroids. Normalized average intensity of NP fluorescence versus tumor spheroid depth, d . The intensity was averaged over all treated spheroids and normalized with the surface intensity. All spheroids were exposed to both nuclear stain (grey, $N=19$) and NPs: Lip (blue, $N=3$), PEG-Lip (red, $N=5$), rHDL (yellow, $N=4$) PNP (green, $N=4$), and LPX (purple, $N=3$). The shaded area corresponds to the tumor spheroid surface and error bars correspond to one SEM

(~24 nm) did not accumulate towards the spheroids' center, though they seemingly also diffused throughout the tumor spheroids. This further confirms that the rHDL distribution in the spheroids is controlled by additional parameters besides size.

Penetration efficiency

To further quantify the ability of the various NPs to penetrate the tumor spheroid, we defined the penetration efficiency as the following ratio:

$$\delta = \frac{1}{N} \sum_{i=1}^N \frac{\langle I \rangle_{in}}{\langle I \rangle_{out}}, \quad (3)$$

where N is the number of spheroids, $\langle I \rangle_{out}$ is the average NP fluorescence at shallow depths ($0 \mu\text{m} < d < 20 \mu\text{m}$), and $\langle I \rangle_{in}$ is the average intensity deeper in the spheroids (60

$\mu\text{m} < d < 80 \mu\text{m}$). A uniform distribution of NPs within the spheroid would yield a δ close to 1 convoluted with an exponential-like decay, due to attenuation of the laser light etc. As the penetration efficiency δ of the nuclear stain reflects the diffusion gradient in combination with the attenuating factors, it can be used to assess the homogeneity between tumor spheroids. The consistent δ values for the nuclear stain (Fig. 5) confirmed that the tumor spheroids are uniform in morphology and size. The penetration efficiency of the NPs (Fig. 5) generally followed the trends observed from the cross-sections (Fig. 3) and penetration profiles (Fig. 4). Only LPX has lower δ than the nuclear stain and significantly lower than both Lip ($p < 0.04$), PEG-Lip ($p = 0.001$), and PNP ($p = 0.002$), since they mainly associate or is taken up by the outermost cells. The rHDL have the highest penetration efficiency δ , which is significantly larger than Lip ($p = 0.02$), nuclear stain and LPX ($p < 0.0001$, both). This is likely due to a combination of their small size, allowing them to easily diffuse through intercellular spaces of the tumor spheroids, and the surprising augmented accumulation of rHDL deeper in the spheroid.

To evaluate if NPs were taken up by the cells or simply adhered to their surface, we imaged the surface cells of the spheroid individually (Fig. 6). As these images shows a single sheet in the imaging stack ($0.4 \mu\text{m}$ thickness) inside the more than $10 \mu\text{m}$ cells, the NP fluorescence (red) measured in proximity to the nucleus (green) are likely to be internalized NPs. These results are indicative of a view, where all NPs are internalized (passively or actively) but to a greater extend for rHDL and LPX compared to Lip and PEG-Lip. Evidently, LPX, rHDL, and Lip were not only taken up by the cells but they also formed aggregations that adhered to the spheroid surface (Fig. 3).

Interestingly, Lip and PEG-Lip show similar uptake by outermost cells (Fig. 6 A,B) and have similar δ ($p = 0.95$), though the $d_{1/2}$ indicated that PEG-Lip penetrated deeper into the spheroid. This can in part be explained by the measured intensity peak of PEG-Lip just beneath the tumor spheroid surface (Fig. 4). Hence, the PEG-Lip apparently overcome adherence to the spheroid surface and penetrate the first cell-layers efficiently, while only a limited amount reach deeper into the spheroid. We speculate that their PEGylation reduces interactions between PEG-Lip and the cell membrane⁶⁸ to allow rapid diffusion through the spheroid^{7,41,69}, in contrast to the less negatively-charged/non-PEGylated Lip and the slightly positively charged LPX.

The effect of NP design on the penetration efficiency

The penetration efficiency is an interplay between NP design, tumor morphology and cell internalization sensitivity^{9,12}. We found that LPX had very different penetration efficiency than Lip and PEG-Lip despite their similar size ($\sim 100 \text{ nm}$). This

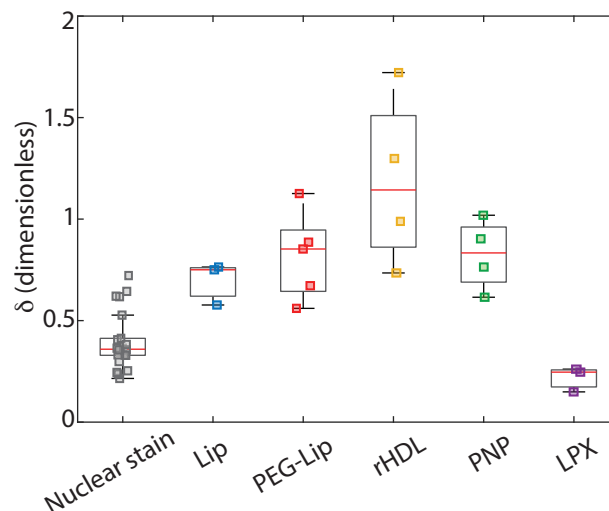


Fig. 5 Box-plot of the penetration efficiency, δ , of nanoparticles in U87-MG tumor spheroids. The penetration efficiency is the ratio between the average fluorescence of the outermost band ($0\text{--}20 \mu\text{m}$ depth) and an inner band ($60\text{--}80 \mu\text{m}$ depth).

might be attributed to the positive surface charge of LPX causing fusion-based uptake by the outermost cells (Fig. 6), and lower stability of the LPX. However, the importance of the surface charge has also been observed in other studies where charged NPs were shown to penetrate less efficiently than neutral NPs^{48,70,71}.

The small differences in sizes of rHDL and PNP ($\sim 10 \text{ nm}$ versus $\sim 24 \text{ nm}$) might contribute to the slightly different penetration efficiencies, where rHDL accumulated more inside the spheroid (Fig. 3 and Fig. 4). We suggest, however, that the great accumulation of rHDL inside the spheroid is attributed to effects from the different environment at the spheroid core relative to the surface, e.g. the slightly acidic environment inside the spheroid might cause rHDL aggregation, or alter the interactions between the rHDL/apoA-I and the extracellular matrix and/or cells⁷². Interestingly, Lee et al.¹¹ showed decreased penetration depth for NPs with targeting ligands, as the NP binding and uptake by the outermost cells inhibited further NP penetration into the spheroid. As SR-BI is expressed by the cells, the rHDL could - in principle - be actively taken up by all cells in the spheroids, thus resulting in likewise decreased accumulation towards the tumor center due to enhanced clearance by the outermost cells, compared to similar sized non-targeting NPs. In contrast, Tang et al.²⁹ suggest that SR-BI receptor-mediated cell uptake of HDL-mimicking NPs in the core of the tumor spheroid is important for enhanced penetration of the NPs. They based this claim on the observation that PEGylation of the HDL-mimicking NPs decreased the penetration into the tumor spheroid, which they attribute

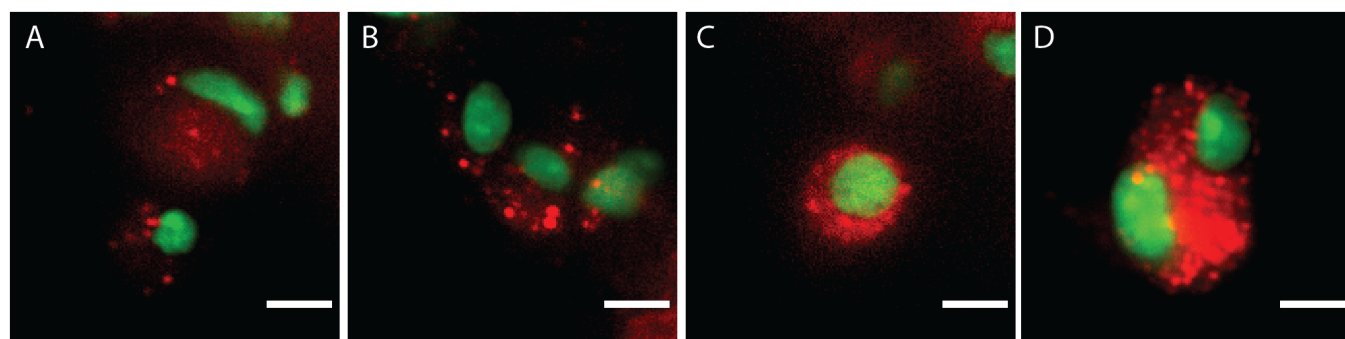


Fig. 6 Uptake of NPs by spheroid surface cells. Representative optical sections of cells on the tumor surface. Overlay pseudo-colored images of nuclear stained cells (green) on the spheroid surface, treated with the various lipid-based NPs (red): PEG-Lip (A:), Lip (B:), rHDL (C:) and LPX (D:). Intensity levels were kept constant and scale bars correspond to 10 μm .

to SR-BI interactions being diminished by PEG. However, we emphasize that SR-BI is expressed throughout the tumor spheroid, and we therefore suggest that additional parameters contribute to the observed increased rHDL accumulation towards the spheroid core.

The penetration efficiency of NPs is an important evaluation measure of therapeutic delivery systems that aim at distributing drugs uniformly in the tumor and must be considered together with the equally important biodistribution of NPs, which determines how much of the intravenously administered NPs ends up in *in vivo* tumor tissue compared to other organs¹⁰. More specifically, PEGylation of liposomes is believed to be very important for long circulation times and results in high accumulation in the tumor due to the expected enhanced permeability and retention (EPR) effect^{3,16}, even though the exact relation between circulation and biodistribution is under much debate (chapter 5 in Ref. 73). We observed only slight (but not significant) difference in the penetration efficiency between Lip and PEG-Lip. In accordance with other *in vitro* studies we observed higher penetration efficiency of the smaller NPs (rHDL and PNP)⁷⁴. In contrast in *in vivo*, ~ 100 nm is believed to be the optimal size for uptake in tumors through the EPR effect⁷⁵. Despite their small size, intravenously injected rHDL is reported to yield relatively high tumor accumulation, often attributed to their SR-BI targeting feature^{29,76–78}. Our results suggest that the rHDL can be retained in the tumor, possibly as a result of the naturally occurring gradients in the cancer spheroid; hence, this might add to the explanation of the enhanced tumor accumulation of rHDL. Consequently, we highlight that the amount of NPs distributed in the tumor tissue is an interplay between NP biodistribution and penetration efficiency.

Conclusion

We performed a head-to-head comparison of penetration efficiencies of lipid-based NPs that varied in size, surface charge, surface chemistry, stability, and targeting ability. Besides the direct comparison between the selected lipid-based NPs, our findings shed light on important and relevant effects associated to the penetration of NPs into tumors. While we only observed limited effect on the penetration efficiency from PEGylation of liposomes, we did observe an effect of the NPs' stability and surface charge, as indicated by the limited penetration efficiency of LPX compared to Lip/PEG-Lip. We also observed a high penetration efficiency for rHDL and speculate that rHDL's unique penetration profile is attributed to a combination of their small size and effects associated to the spheroid environment, e.g. lower pH.

The used of light-sheet microscopy and the detailed image analysis can easily be adapted to screen the penetration efficiency of any fluorescent NPs in 3D tumor spheroids. Thus, we present a powerful tool and analysis method for *in vitro* evaluation of the penetration efficiency of NPs; a measure that can be highly relevant for the therapeutic effect of the corresponding drug delivery system.

Materials and Methods

Preparation of NPs

Materials: The lipids 1,2-dipalmitoyl-sn-glycero-3-phosphocholine (DPPC), cholesterol, 1,2-dioleoyl-3-trimethylammonium-propane (chloride salt); (DOTAP) and 1,2-dioleoyl-sn-glycero-3-phosphoethanolamine-N-[amino(polyethylene glycol)-2000] (ammonium salt); (DOPE-PEG2k) were supplied from Avanti Polar Lipids (USA). The lipophilic carbocyanine dye 1,1'-Diocadecyl-3,3,3',3'-Tetramethylindocarbocyanine Perchlorate (DiI) was supplied from Thermo Fisher Scientific (USA). The

CpG ODN2395 were supplied from Invivogen (USA). The stealth liposome mix (consisting of hydrogenated soy L- α -phosphatidylcholine (HSPC), cholesterol, and DSPE-PEG2k in a weight ratio of 3:1:1) was acquired from Lipoid GmbH (Germany). Reagents for the buffers used for preparation of the NPs (Phosphate Buffered Saline (PBS), sodium chloride, sodium citrate and, hepes, glucose, sodium cholate hydrate), 99.9% absolute ethanol and *tert*-Butanol were all supplied from Sigma-Aldrich (Denmark).

Liposomes / PEGylated Liposomes: Lip were prepared with DPPC:Cholesterol:DiI in a molar ratio of (61.3:38.2:0.5), while PEG-Lip were prepared from the stealth liposome mix HSPC:Cholesterol:DSPE-PEG (56.6:38.2:5.2) supplied with 0.5 mol% DiI. Initially, the lipids were dissolved in *tert*-butanol:MilliQ (9:1), snap-frozen in liquid nitrogen and freeze-dried overnight using a Scanvac Coolsafe lyophilizer (Labogene, Denmark). The dry lipids were re-hydrated in PBS to a total lipid concentration of 10 mM and put under 65 °C heating and magnet stirring for 1 hour. The size of the liposomes was controlled by extruding 21 times through Whatman filters (GE Healthcare, UK) with a pore size of 100 nm using a Mini-Extruder from Avanti Polar Lipids. The liposome suspension was transferred to a glass vial and stored at 4 °C.

Lipoplexes: LPX were prepared by ethanol injection method. They were formulated with cholesterol:DOTAP:DOPE-PEG2k:DiI (49.5:49:1:0.5) and CpG ODN 2395 (single-stranded synthetic DNA) as the encapsulated nucleic acid. Initially, the lipids were dissolved in 99.9% absolute ethanol, and CpG was diluted in citrate buffer, pH 5. The lipid solution was mixed into the CpG solution under vigorous vortexing yielding a DOTAP:CpG (8:1). Immediately after mixing, the mixture was diluted by adding twice the volume of buffered saline (0.3 M sodium chloride, 20 mM sodium citrate, pH 6.0). To remove excess ethanol, the solution was then dialyzed for 24 hours using cassettes with 3.5K MWCO, (Thermo Fisher Scientific, USA) against 300 mM Hepes 5% Glucose buffer (pH 7.4) with two buffer exchanges. After dialysis, the LPX solution was transferred to amicon spin filters (MWCO 10000) in 15 mL tubes and centrifuged three times at 4000 g, 4 °C for 10 min. Between each cycle, the volume was replenished by adding 300 mM Hepes, 5% Glucose buffer (pH 7.4) to ensure removal of unbound CpG. After washing, the LPX solution (10 mM total lipid concentration) was transferred to a new vial and allowed to equilibrate at RT for 30 min. The LPX were stored at 4 °C and used within 4 weeks after preparation.

rHDL: The lipids DPPC:DiI (99.5:0.5) were dissolved in *tert*-butanol:MilliQ (9:1) before freeze-drying the lipids overnight. ApoA-I (purified from human plasma as described

elsewhere¹⁸) dissolved in PBS containing 20 mM cholate was added to the lipid mixture such that it yielded a protein:lipid molar ratio of 100 and a total lipid concentration of 5 mM. The solution were heated to 41 °C for approximately 1 hour to ensure that the lipids dissolved. Subsequently, Bio-Beads™ from Bio-Rad (Denmark) were added to remove the cholate and induce self-assembly of the rHDL. The sample were incubated overnight with the Bio-Beads™, and the Bio-Beads™ were removed by spinning the liquid from an 2 mL Eppendorf tube with an perforated hole into a falcon tube. The sample was stored at 4 °C before use.

Characterization of the NPs

All lipid-based NPs were fluorescently-labeled using 0.5 mol% DiI fluorophore (549/565). They were diluted in PBS, such that they contained similar amount of fluorophores, as estimated by absorbance (NanoDrop 2000/2000c Spectrophotometer, Thermo Fisher Scientific), (Supplementary Information Fig. S2), and were further diluted 10 \times in imaging medium (see Sample preparation section) when added to the spheroids.

The fluorescently-labeled (580/605 nm) anionic polystyrene carboxylate-modified nanoparticles (ThermoFisher, Lot Number = 1922891) were sonicated for 10 min and were diluted in imaging medium (see Sample preparation section) to a final concentration of 1.7×10^{11} particles/mL.

The hydrodynamic diameters of the NPs were measured by dynamic light scattering (DLS) on a ZetaSizer Nano ZS (Malvern Instruments, UK) over an average of 3 runs of 10-15 cycles. The results were estimated by number [%]. The zeta potential was obtained by the same instrument using a universal 'Dip' Cell (Malvern Panalytical, UK) and was estimated with an average of 3 runs with an automatically determined number of cycles (10-100 cycles). Before the zeta potential measurements, the samples were diluted 25 \times in a buffer containing 10 mM HEPES and 5% glucose (pH 7.4). For both the size and zeta potential measurements a distribution is obtained from each run/cycle with mean and SD. In Table 1, we present the average of the means and average of the SD from the three runs.

Cell culture

Gliosblastoma multiform U87-MG cell were cultured in high glucose Dulbecco's modified Eagle Medium (DMEM) supplemented with 10% Fetal Bovine Serum (FBS) and 1% (100 units/mL penicillin and 100 μ g/mL streptomycin). All from Gibco™.

Gravitation-assisted spheroid formation: 5×10^4 cells/mL were seeded in round-bottom ultra-low attachment 96 wells (Corning Costar) in a volume of 100 μ l DMEM per well and

incubated for 72 hours (37° C, 5% CO₂, and 100% humidity). After 72 hours, the spheroids reached a radius of $134 \pm 10 \mu\text{m}$ (mean \pm SD, N=19).

Sample preparation

For imaging, culture medium was replaced by phenol red-free DMEM (FluoroBrite™, Gibco) without serum, to minimize noise. Fully-formed spheroids were rinsed 3 times with imaging medium and were treated with nanoparticles, in fresh imaging medium, for 5 hours. After 3 hours of incubation, the spheroids were nuclear-labelled, by supplementing the wells with a cell-permeable nucleic acid stain (SYTO13, Invitrogen; 488/509 nm). Although the nuclear stain is a high performance dye, it causes photo-toxicity within 3 hours⁷⁹, which restricts live-cell imaging. Spheroids were washed 3 times in PBS (Gibco™) and were then immersed in fresh imaging medium. The spheroids were embedded in 1% low-melt agarose (NuSieve GTG Agarose; Lonza, Rockland, ME, USA), were transferred separately in fluorinated ethylene propylene (FEP) tubes (inner diameter 0.8 mm, outer diameter 1.6 mm) (Bohler) and were mounted on the microscope.

Live spheroid imaging

We used an Aurora airy light sheet microscope (M Squared) with M2 filter cube with an objective for illumination (UMPlanFL N 10 \times /0.30 W) and one for detection (UMPlanFL N 20 \times /0.50 W) each with 3.5 mm working distance. The light sheet is equipped with a blue (488 nm) and a yellow (570 nm) laser. The light sheet allows deep sample penetration and high axial resolution over an extended field of view (600 mm \times 600 mm). Emitted light was collected through a band-pass filter (520 – 540 nm) and low-pass filter (< 570 nm) for the 488 nm and 561 nm laser beams, respectively. Two stacks of images were recorded sequentially, one for the nuclear stain and one for the nanoparticle stain in steps of 0.4 μm in the axial direction by use of the build Aurora Alpha acquisition software. Laser intensity and exposure was kept constant among experiments, which were performed in room temperature with minimized background light.

Image analysis

To measure the fluorescence intensity versus depth of the spheroid we analyzed cross sections and quantified the intensity with a combination of Fiji plugins and custom-made Matlab-routines. As our spheroids on average were 300 μm in diameter and the step size in the axial-direction was 0.4 μm , the measured intensity of our cross sections were averaged over 100 frames (which corresponds to 40 μm). We estimated the variation of the radius over this band to be less than

the variations in R_θ in the imaging plane. The obtained average cross sections were analyzed to obtain the mean intensities as in equation 1.

Statistics: Unless otherwise stated, data are shown as mean \pm standard deviation (SD) or SD of the mean (SDM), $N \geq 3$. To assess statistical significance, analysis of variance (ANOVA, one-way) was performed, for comparison of means, followed by Tukey's post hoc test. Upon comparison to the alpha level of 5%, a p-value of < 0.05 was considered statistically significant.

Acknowledgement

LJ acknowledges funding from the Danish National Research Council (DNRF116) and fruitful discussions with Lene Oddershede and Petra Hammerlik. MN thanks Younes Farhangibarooji for his valuable help with the light-sheet microscope.

Author contributions

MN did the spheroid growth and imaging as well as data analysis under the supervision of LJ. RM, MFV and DP synthesized and characterized the lipid-based particles under the supervision of TLA and JBS. MN, DP, JBS and LJ discussed the results and wrote the majority of the manuscript. All authors read and approved the submitted manuscript.

References

- 1 Wang, A. Z.; Langer, R.; Farokhzad, O. C. Nanoparticle Delivery of Cancer Drugs. *Annual Review of Medicine* **2012**, 63, 185–198.
- 2 Puri, A.; Loomis, K.; Smith, B.; Lee, J. H.; Yavlovich, A.; Heldman, E.; Blumenthal, R. Lipid-based nanoparticles as pharmaceutical drug carriers: From concepts to clinic. *Critical Reviews in Therapeutic Drug Carrier Systems* **2009**, 26, 523–580.
- 3 Yingchoncharoen, P.; Kalinowski, D. S.; Richardson, D. R. Lipid-based drug delivery systems in cancer therapy: What is available and what is yet to come. *Pharmacological Reviews* **2016**, 68, 701–787.
- 4 Allen, T. M.; Cullis, P. R. Drug Delivery Systems: Entering the Mainstream. *Science* **2004**, 303, 1818–1822.
- 5 Senapati, S.; Mahanta, A. K.; Kumar, S.; Maiti, P. Controlled drug delivery vehicles for cancer treatment and their performance. *Signal transduction and targeted therapy* **2018**, 3, 1–19.
- 6 Barenholz, Y. Doxil® - The first FDA-approved nano-drug: Lessons learned. *Journal of Controlled Release* **2012**, 160, 117–134.

- 7 Tchoryk, A.; Taresco, V.; Argent, R. H.; Ashford, M.; Gellert, P. R.; Stolnik, S.; Grabowska, A.; Garnett, M. C. Penetration and Uptake of Nanoparticles in 3D Tumor Spheroids. *Bioconjugate Chemistry* **2019**, *30*, 1371–1384.
- 8 Li, L.; Sun, J.; He, Z. Deep Penetration of Nanoparticulate Drug Delivery Systems into Tumors: Challenges and Solutions. *Current Medicinal Chemistry* **2013**, *20*, 2881–2891.
- 9 Cabral, H.; Matsumoto, Y.; Mizuno, K.; Chen, Q.; Murakami, M.; Kimura, M.; Terada, Y.; Kano, M. R.; Miyazono, K.; Uesaka, M.; others, Accumulation of sub-100 nm polymeric micelles in poorly permeable tumours depends on size. *Nature nanotechnology* **2011**, *6*, 815.
- 10 Perrault, S. D.; Walkey, C.; Jennings, T.; Fischer, H. C.; Chan, W. C. W. Mediating tumor targeting efficiency of nanoparticles through design. *Nano letters* **2009**, *9*, 1909–1915.
- 11 Lee, H.; Fonge, H.; Hoang, B.; Reilly, R. M.; Allen, C. The effects of particle size and molecular targeting on the intratumoral and subcellular distribution of polymeric nanoparticles. *Molecular pharmaceutics* **2010**, *7*, 1195–1208.
- 12 Ernsting, M. J.; Murakami, M.; Roy, A.; Li, S.-D. Factors controlling the pharmacokinetics, biodistribution and intratumoral penetration of nanoparticles. *Journal of controlled release* **2013**, *172*, 782–794.
- 13 Cullis, P. R.; Hope, M. J. Lipid Nanoparticle Systems for Enabling Gene Therapies. *Molecular Therapy* **2017**, *25*, 1467–1475.
- 14 Simonsen, J. B. Evaluation of reconstituted high-density lipoprotein (rHDL) as a drug delivery platform—a detailed survey of rHDL particles ranging from biophysical properties to clinical implications. *Nanomedicine: Nanotechnology, Biology and Medicine* **2016**, *12*, 2161–2179.
- 15 Münter, R.; Kristensen, K.; Pedersbæk, D.; Larsen, J. B.; Simonsen, J. B.; Andresen, T. L. Dissociation of fluorescently labeled lipids from liposomes in biological environments challenges the interpretation of uptake studies. *Nanoscale* **2018**, *10*, 22720–22724.
- 16 Allen, T. M. Liposomal Drug Formulations. *Drugs* **1998**, *56*, 747–756.
- 17 Pedersbæk, D.; Jønsson, K.; Madsen, D. V.; Weller, S.; Bohn, A. B.; Andresen, T. L.; Simonsen, J. B. A quantitative ex vivo study of the interactions between reconstituted high-density lipoproteins and human leukocytes. *RSC Advances* **2020**, *10*, 3884–3894.
- 18 Pedersbæk, D.; Kræmer, M. K.; Kempen, P. J.; Ashley, J.; Braesch-Andersen, S.; Andresen, T. L.; Simonsen, J. B. The composition of reconstituted high-density lipoproteins (rHDL) dictates the degree of rHDL cargo- and size-remodeling via direct interactions with endogenous lipoproteins. *Bioconjugate Chemistry* **2019**, *30*, 2634–2646.
- 19 Berney, E.; Sabnis, N.; Panchoo, M.; Raut, S.; Dickerman, R.; Lacko, A. G. The SR-B1 Receptor as a Potential Target for Treating Glioblastoma. *Journal of Oncology* **2019**, *2019*, 1–10.
- 20 Jiang, Y.; Pjesivac-Grbovic, J.; Cantrell, C.; Freyer, J. P. A multiscale model for avascular tumor growth. *Biophysical Journal* **2005**, *89*, 3884–3894.
- 21 Deisboeck, T. S.; Berens, M. E.; Kansal, A. R.; Torquato, S.; Stemmer-Rachamimov, A. O.; Chiocca, E. A. Pattern of self-organization in tumour systems: complex growth dynamics in a novel brain tumour spheroid model. *Cell proliferation* **2001**, *34*, 115–134.
- 22 Amaral, R. L. F.; Miranda, M.; Marcato, P. D.; Swiech, K. Comparative analysis of 3D bladder tumor spheroids obtained by forced floating and hanging drop methods for drug screening. *Frontiers in physiology* **2017**, *8*, 605.
- 23 Mittler, F.; Obeid, P.; Rulina, A. V.; Haguët, V.; Gidrol, X.; Balakirev, M. Y. High-Content Monitoring of Drug Effects in a 3D Spheroid Model. *Frontiers in Oncology* **2017**, *7*, 293.
- 24 Sant, S.; Johnston, P. A. The production of 3D tumor spheroids for cancer drug discovery. *Drug Discovery Today: Technologies* **2017**, *23*, 27–36.
- 25 Hirschhaeuser, F.; Menne, H.; Dittfeld, C.; West, J.; Mueller-Klieser, W.; Kunz-Schughart, L. A. Multicellular tumor spheroids: an underestimated tool is catching up again. *Journal of biotechnology* **2010**, *148*, 3–15.
- 26 Lazzari, G.; Vinciguerra, D.; Balasso, A.; Nicolas, V.; Goudin, N.; Garfa-Traore, M.; Fehér, A.; Dinnyés, A.; Nicolas, J.; Couvreur, P.; Mura, S. Light sheet fluorescence microscopy versus confocal microscopy: in quest of a suitable tool to assess drug and nanomedicine penetration into multicellular tumor spheroids. *European Journal of Pharmaceutics and Biopharmaceutics* **2019**, *142*, 195–203.
- 27 Cutrona, M. B.; Simpson, J. C. A High-Throughput Automated Confocal Microscopy Platform for Quantitative Phenotyping of Nanoparticle Uptake and Transport in Spheroids. *Small* **2019**, *15*, 1–14.
- 28 Darrigues, E.; Nima, Z. A.; Nedosekin, D. A.; Watanabe, F.; Alghazali, K. M.; Zharov, V. P.; Biris, A. S. Tracking Gold Nanorods' Interaction with Large 3D Pancreatic-Stromal Tumor Spheroids by Multimodal Imaging: Fluorescence, Photoacoustic, and Photothermal Microscopies. *Scientific Reports* **2020**, *10*, 3362.
- 29 Tang, J.; Kuai, R.; Yuan, W.; Drake, L.; Moon, J. J.; Schwendeman, A. Effect of size and pegylation of liposomes and peptide-based synthetic lipoproteins on tumor targeting. *Nanomedicine: Nanotechnology, Biology, and*

- 30 Zhang, L.; Wang, Y.; Yang, D.; Huang, W.; Hao, P.; Feng, S.; Appelhans, D.; Zhang, T.; Zan, X. Shape effect of nanoparticles on tumor penetration in monolayers versus spheroids. *Molecular Pharmaceutics* **2019**, *16*, 2902–2911.
- 31 Mollo, V.; Scognamiglio, P.; Marino, A.; Ciofani, G.; Santoro, F. Probing the Ultrastructure of Spheroids and Their Uptake of Magnetic Nanoparticles by FIB–SEM. *Advanced Materials Technologies* **2020**, 1900687.
- 32 Carver, K.; Ming, X.; Juliano, R. L. Multicellular tumor spheroids as a model for assessing delivery of oligonucleotides in three dimensions. *Molecular Therapy - Nucleic Acids* **2014**, *3*, e153.
- 33 El-Dakdouki, M. H.; Puré, E.; Huang, X. Development of drug loaded nanoparticles for tumor targeting. Part 2: Enhancement of tumor penetration through receptor mediated transcytosis in 3D tumor models. *Nanoscale* **2013**, *5*, 3904–3911.
- 34 Agarwal, R.; Journey, P.; Raythatha, M.; Singh, V.; Sreenivasan, S. V.; Shi, L.; Roy, K. Effect of shape, size, and aspect ratio on nanoparticle penetration and distribution inside solid tissues using 3D spheroid models. *Advanced healthcare materials* **2015**, *4*, 2269–2280.
- 35 Arakawa, A.; Jakubowski, N.; Koellensperger, G.; Theiner, S.; Schweikert, A.; Flemig, S.; Iwahata, D.; Traub, H.; Hirata, T. Quantitative Imaging of Silver Nanoparticles and Essential Elements in Thin Sections of Fibroblast Multicellular Spheroids by High Resolution Laser Ablation Inductively Coupled Plasma Time-of-Flight Mass Spectrometry. *Analytical chemistry* **2019**, *91*, 10197–10203.
- 36 Fleddermann, J.; Susewind, J.; Peuschel, H.; Koch, M.; Tavernaro, I.; Kraegeloh, A. Distribution of SiO₂ nanoparticles in 3D liver microtissues. *International journal of nanomedicine* **2019**, *14*, 1411.
- 37 Durymanov, M.; Kroll, C.; Permyakova, A.; Reineke, J. Role of Endocytosis in Nanoparticle Penetration of 3D Pancreatic Cancer Spheroids. *Molecular Pharmaceutics* **2019**, *16*, 1074–1082.
- 38 Olsen, T. R.; Mattix, B.; Casco, M.; Herbst, A.; Williams, C.; Tarasidis, A.; Evans, G.; Jenkins, L.; McMahon, C. L.; Simionescu, D.; Visconti, R. P.; Alexis, F. Processing cellular spheroids for histological examination. *Journal of Histotechnology* **2014**, *37*, 138–142.
- 39 Lu, H.; Su, J.; Mamdooh, R.; Li, Y.; Stenzel, M. H. Cellular Uptake of Gold Nanoparticles and Their Movement in 3D Multicellular Tumor Spheroids: Effect of Molecular Weight and Grafting Density of Poly(2-hydroxyl ethyl acrylate). *Macromolecular Bioscience* **2020**, *20*, 1–11.
- 40 Priwitaningrum, D. L.; Blondé, J.-B. G.; Sridhar, A.; van Baarlen, J.; Hennink, W. E.; Storm, G.; Le Gac, S.; Prakash, J. Tumor stroma-containing 3D spheroid arrays: A tool to study nanoparticle penetration. *Journal of controlled release* **2016**, *244*, 257–268.
- 41 Huang, K.; Boerhan, R.; Liu, C.; Jiang, G. Nanoparticles penetrate into the multicellular spheroid-on-chip: effect of surface charge, protein corona, and exterior flow. *Molecular pharmaceutics* **2017**, *14*, 4618–4627.
- 42 Lee, J.; Lilly, G. D.; Doty, R. C.; Podsiadlo, P.; Kotov, N. A. In vitro toxicity testing of nanoparticles in 3D cell culture. *Small* **2009**, *5*, 1213–1221.
- 43 Leite, P. E. C.; Pereira, M. R.; Harris, G.; Pamies, D.; Dos Santos, L. M. G.; Granjeiro, J. M.; Hogberg, H. T.; Hartung, T.; Smirnova, L. Suitability of 3D human brain spheroid models to distinguish toxic effects of gold and poly-lactic acid nanoparticles to assess biocompatibility for brain drug delivery. *Particle and fibre toxicology* **2019**, *16*, 22.
- 44 Jiang, X.; Xin, H.; Gu, J.; Xu, X.; Xia, W.; Chen, S.; Xie, Y.; Chen, L.; Chen, Y.; Sha, X. Solid tumor penetration by integrin-mediated pegylated poly (trimethylene carbonate) nanoparticles loaded with paclitaxel. *Biomaterials* **2013**, *34*, 1739–1746.
- 45 Kankala, R. K.; Liu, C.-G.; Yang, D.-Y.; Wang, S.-B.; Chen, A.-Z. Ultrasmall platinum nanoparticles enable deep tumor penetration and synergistic therapeutic abilities through free radical species-assisted catalysis to combat cancer multidrug resistance. *Chemical Engineering Journal* **2020**, 383, 123138.
- 46 Skobeltsin, A.; Farrakhova, D.; Maklygina, Y.; Romanishkin, I.; Ryabova, A.; Yakovets, I.; Millard, M.; Boline, L.; Plyutinskaya, A.; Karmakova, T. 3D spheroid cultures for evaluation of nanophotosensitizers accumulation. *Journal of Physics: Conference Series*. 2020; p 12032.
- 47 Mellor, H.; Davies, L. Optimising non-viral gene delivery in a tumour spheroid model. 2006; <http://onlinelibrary.wiley.com/doi/10.1002/jgm.947/full>.
- 48 Kostarelos, K.; Emfietzoglou, D.; Papakostas, A.; Yang, W. H.; Ballangrud, Å.; Sgouros, G. Binding and interstitial penetration of liposomes within avascular tumor spheroids. *International Journal of Cancer* **2004**, *112*, 713–721.
- 49 Kou, L.; Yao, Q.; Sivaprakasam, S.; Luo, Q.; Sun, Y.; Fu, Q.; He, Z.; Sun, J.; Ganapathy, V. Dual targeting off-carnitine-conjugated nanoparticles to octn2 and ATB⁺ to deliver chemotherapeutic agents for colon cancer therapy. *Drug Delivery* **2017**, *24*, 1338–1349.
- 50 Williams, Y.; Byrne, S.; Bashir, M.; Davies, A.; Whelan, A.; Gunko, Y.; Kelleher, D.; Volkov, Y. Comparison of three cell fixation methods for high content analysis assays utilizing quantum dots. *Journal of Microscopy* **2008**,

- 232, 91–98.
- 51 He, Y.; Laugesen, K.; Kamp, D.; Sultan, S. A.; Oddershede, L. B.; Jauffred, L. Effects and side effects of plasmonic photothermal therapy in brain tissue. *Cancer Nanotechnology* **2019**, *10*, 8.
- 52 Tomer, R.; Khairy, K.; Amat, F.; Keller, P. J. Quantitative high-speed imaging of entire developing embryos with simultaneous multiview light-sheet microscopy. *Nature methods* **2012**, *9*, 755–63.
- 53 Vettenburg, T.; Dalgarno, H. I. C.; Nytk, J.; Coll-Lladó, C.; Ferrier, D. E. K.; Čížmár, T.; Gunn-Moore, F. J.; Dholakia, K. Light-sheet microscopy using an Airy beam. *Nature methods* **2014**, *11*, 541.
- 54 Andilla, J.; Jorand, R.; Olarte, O. E.; Dufour, A. C.; Cazales, M.; Montagner, Y. L. E.; Ceolato, R.; Riviere, N.; Olivo-Marin, J.-C.; Loza-Alvarez, P.; Lorenzo, C. Imaging tissue-mimic with light sheet microscopy: A comparative guideline. *Scientific Reports* **2017**, *7*, 44939.
- 55 Verveer, P. J.; Swoger, J.; Pampaloni, F.; Greger, K.; Marcello, M.; Stelzer, E. H. High-resolution three-dimensional imaging of large specimens with light sheet-based microscopy. *Nature Methods* **2007**, *4*, 311–313.
- 56 Langhans, S. A. Three-dimensional in vitro cell culture models in drug discovery and drug repositioning. *Frontiers in pharmacology* **2018**, *9*, 6.
- 57 Vinci, M.; Gowan, S.; Boxall, F.; Patterson, L.; Zimmermann, M.; Court, W.; Lomas, C.; Mendiola, M.; Hardisson, D.; Eccles, S. A. Advances in establishment and analysis of three-dimensional tumor spheroid-based functional assays for target validation and drug evaluation. *BMC Biology* **2012**, *10*, 29.
- 58 Münter, R.; Kristensen, K.; Pedersbæk, D.; Andresen, T. L.; Simonsen, J. B.; Larsen, J. B. *Nanotechnology Characterization Tools for Tissue Engineering and Medical Therapy*; Springer Berlin Heidelberg: Berlin, Heidelberg, 2019; pp 333–359.
- 59 Semple, S. C.; Klimuk, S. K.; Harasym, T. O.; Dos Santos, N.; Ansell, S. M.; Wong, K. F.; Maurer, N.; Stark, H.; Cullis, P. R.; Hope, M. J.; Scherrer, P. Efficient encapsulation of antisense oligonucleotides in lipid vesicles using ionizable aminolipids: Formation of novel small multilamellar vesicle structures. *Biochimica et Biophysica Acta - Biomembranes* **2001**, *1510*, 152–166.
- 60 Leung, A. K.; Tam, Y. Y. C.; Cullis, P. R. *Advances in Genetics*; Elsevier, 2014; Vol. 88; pp 71–110.
- 61 Holland, J. W.; Hui, C.; Cullis, P. R.; Madden, T. D. Poly(ethylene glycol)-lipid conjugates regulate the calcium-induced fusion of liposomes composed of phosphatidylethanolamine and phosphatidylserine. *Biochemistry* **1996**, *35*, 2618–2624.
- 62 Pattni, B. S.; Chupin, V. V.; Torchilin, V. P. New developments in liposomal drug delivery. *Chemical reviews* **2015**, *115*, 10938–10966.
- 63 Bendix, P. M.; Reihani, S. N. S.; Oddershede, L. B. Direct Measurements of Heating by Electromagnetically Trapped Gold Bilayers. *ACS Nano* **2010**, *4*, 2256–2262.
- 64 Cavigliolo, G.; Shao, B.; Geier, E. G.; Ren, G.; Heinecke, J. W.; Oda, M. N. The interplay between size, morphology, stability, and functionality of high-density lipoprotein subclasses. *Biochemistry* **2008**, *47*, 4770–4779.
- 65 Kim, J. S.; Kang, Y.; Son, K. H.; Choi, S. M.; Kim, K. Y. Manufacturing and shelf stability of reconstituted high-density lipoprotein for infusion therapy. *Biotechnology and Bioengineering* **2011**, *16*, 785–792.
- 66 Nunes, A. S.; Barros, A. S.; Costa, E. C.; Moreira, A. F.; Correia, I. J. 3D tumor spheroids as in vitro models to mimic in vivo human solid tumors resistance to therapeutic drugs. *Biotechnology and Bioengineering* **2019**, *116*, 206–226.
- 67 Nguyen, S. D.; Öörni, K.; Lee-Rueckert, M.; Pihlajamäa, T.; Metso, J.; Jauhainen, M.; Kovanen, P. T. Spontaneous remodeling of HDL particles at acidic pH enhances their capacity to induce cholesterol efflux from human macrophage foam cells. *Journal of Lipid Research* **2012**, *53*, 2115–2125.
- 68 Torchilin, V. P.; Klibanov, A. L.; Huang, L.; O'Donnell, S.; Nossiff, N. D.; Khaw, B. A. Targeted accumulation of polyethylene glycol-coated immunoliposomes in infarcted rabbit myocardium. *The FASEB journal* **1992**, *6*, 2716–2719.
- 69 Kim, B.; Han, G.; Toley, B. J.; Kim, C.-k.; Rotello, V. M.; Forbes, N. S. Tuning payload delivery in tumour cylinders using gold nanoparticles. *Nature nanotechnology* **2010**, *5*, 465.
- 70 Lieleg, O.; Baumgärtel, R. M.; Bausch, A. R. Selective filtering of particles by the extracellular matrix: An electrostatic bandpass. *Biophysical Journal* **2009**, *97*, 1569–1577.
- 71 Nomura, T.; Koreeda, N.; Yamashita, F.; Takakura, Y.; Hashida, M. Effect of particle size and charge on the disposition of lipid carriers after intratumoral injection into tissue-isolated tumors. *Pharmaceutical Research* **1998**, *15*, 128–132.
- 72 Ramella, N. A.; Rimoldi, O. J.; Prieto, E. D.; Schinella, G. R.; Sanchez, S. A.; Jaureguiberry, M. S.; Vela, M. E.; Ferreira, S. T.; Tricerri, M. A. Human apolipoprotein A-I-derived amyloid: Its association with atherosclerosis. *PLoS ONE* **2011**, *6*.
- 73 Jauffred, L.; Samadi, A.; Klingberg, H.; Bendix, P. M.; Oddershede, L. B. Plasmonic Heating of Nanostructures. *Chemical Reviews* **2019**, *acs.chemrev.8b00738*.

-
- 74 Schleh, C.; Semmler-Behnke, M.; Lipka, J.; Wenk, A.; Hirn, S.; Schäffler, M.; Schmid, G.; Simon, U.; Kreyling, W. G. Size and surface charge of gold nanoparticles determine absorption across intestinal barriers and accumulation in secondary target organs after oral administration. *Nanotoxicology* **2012**, *6*, 36–46.
- 75 Li, S.-D.; Huang, L.; Nanoparticles, B. Pharmacokinetics and biodistribution of nanoparticles. *Molecular pharmaceuticals* **2008**, *5*, 496–504.
- 76 Zhang, Z.; Chen, J.; Ding, L.; Jin, H.; Lovell, J. F.; Corbin, I. R.; Cao, W.; Lo, P. C.; Yang, M.; Tsao, M. S.; Luo, Q.; Zheng, G. HDL-mimicking peptide-lipid nanoparticles with improved tumor targeting. *Small* **2010**, *6*, 430–437.
- 77 Perez-Medina, C.; Tang, J.; Abdel-Atti, D.; Hogstad, B.; Merad, M.; Fisher, E. A.; Fayad, Z. A.; Lewis, J. S.; Mulder, W. J. M.; Reiner, T. PET Imaging of Tumor-Associated Macrophages with ⁸⁹Zr-Labeled High-Density Lipoprotein Nanoparticles. *Journal of Nuclear Medicine* **2015**, *56*, 1272–1277.
- 78 Kuai, R.; Subramanian, C.; White, P. T.; Timmermann, B.; Moon, J. J.; Cohen, M.; Schwendeman, A. Synthetic high-density lipoprotein nanodisks for targeted withalongoide delivery to adrenocortical carcinoma. *International Journal of Nanomedicine* **2017**, *Volume 12*, 6581–6594.
- 79 Hubbard, K. S.; Gut, I. M.; Scheeler, S. M.; Lyman, M. E.; McNutt, P. M. Compatibility of SYTO 13 and Hoechst 33342 for longitudinal imaging of neuron viability and cell death. *BMC research notes* **2012**, *5*, 437.

Supplementary Information

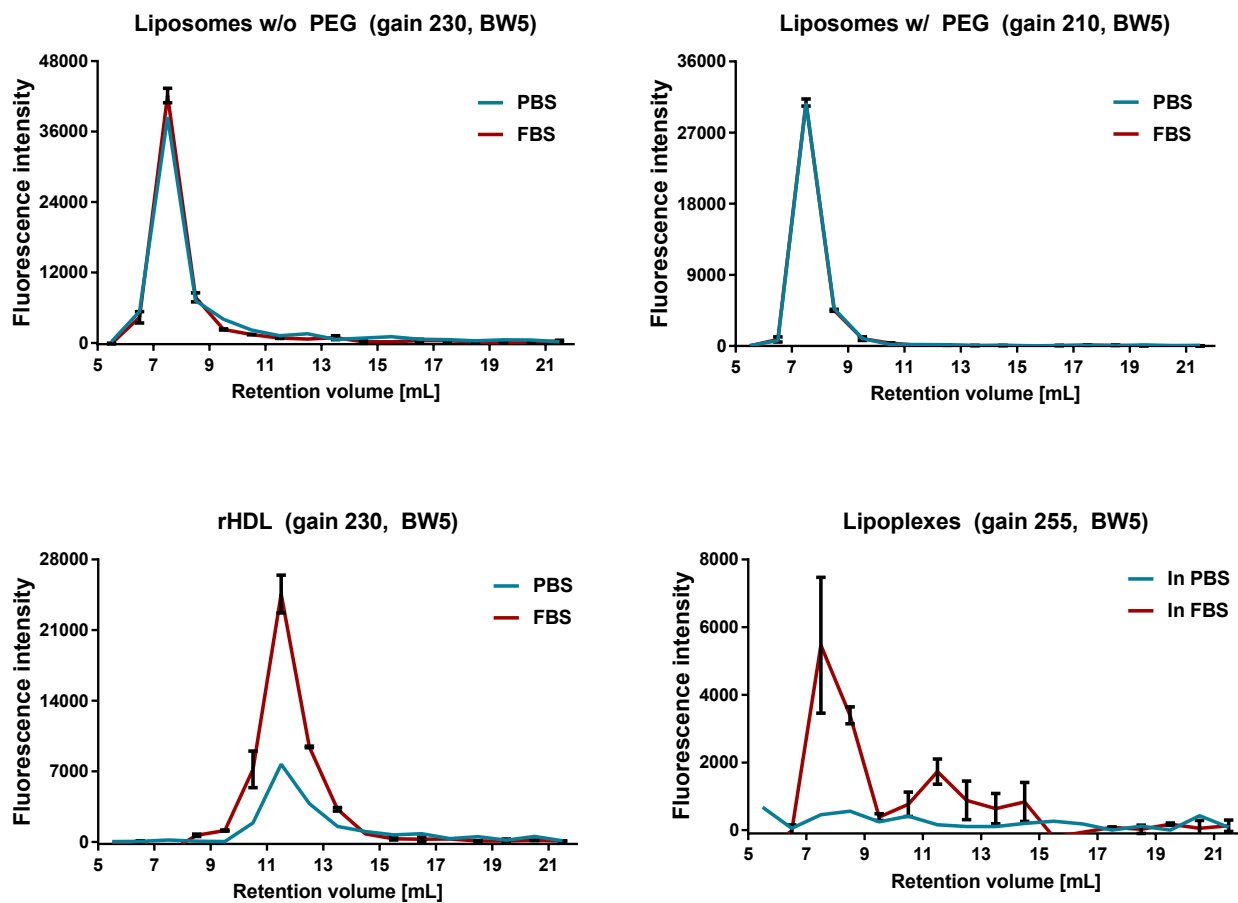
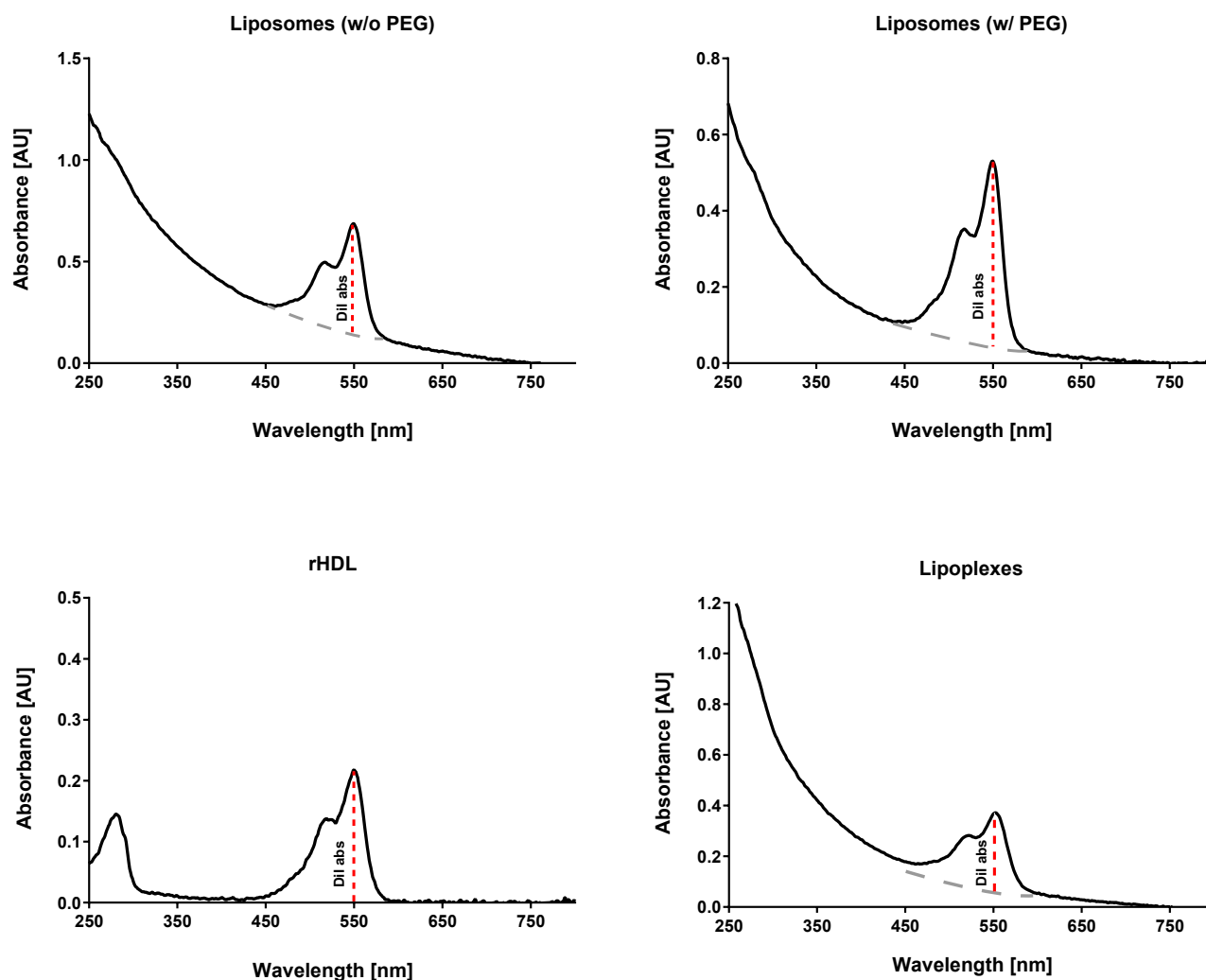


Fig. S1 Estimation of the dynamics of the lipid-conjugated fluorophore-label incorporated into the lipid-based NPs. The NPs were incubated for 3 hours in either PBS or FBS before separating the serum components by size exclusion chromatography using a Superdex 200 Increase 300/10 GL (GE healthcare) on a HPLC system from Shimazu. The fluorescence from the DiI fluorophore was measured by a TECAN Spark microplate reader (TECAN) using excitation wavelength of 549 nm and emission wavelength of 650 nm, both with a bandwidth of 5. The used gains are listed for each NP. The method is similar to what have been described elsewhere^{15,18,58}. The DiI seems relatively stably incorporated. Apparently, the lipoplexes do not elute in PBS, possible due to self-aggregation after being loaded onto the column, thus not being able to pass through the filter on the column. Hence, the signal observed for lipoplexes in FBS could correspond to fluorophore desorbed to serum components. However, this might only be a minor amount, and we emphasize the tumor penetration experiments was conducted in serum-free medium, thereby minimizing effects caused by fluorophore desorption to serum components.



Samples	Abs @549 nm	DiI abs @549	Dilution
Liposomes (w/o PEG)	0,681	0,531	17,1
Liposomes (w/ PEG)	0,522	0,472	15,2
rHDL	0,217	0,217	7,0
Lipoplexes	0,354	0,274	8,8

Fig. S2 Determination of the dilution of NPs required to obtain equal amount of fluorophore in the samples, which was estimated using absorbance. The absorbance was measured on NanoDrop 2000/2000c Spectrophotometer (Thermo Fisher Scientific). The absorbance at 549 nm can be a combination of absorbance from the fluorophore DiI and scattering from the NPs. Hence, we distinguished between scattering and fluorophore absorbance by utilizing the scattering profiles as illustrated on the representative absorbance spectra from the NPs (in PBS). Due to their smaller size rHDL did have not any absorbance from scattering at 549 nm. In the table the average absorbance from minimum three measurements are listed along with the determined DiI absorbance after subtracting scattering and the dilution (in PBS) used to obtain equal DiI concentration in the samples. Note that the samples were further diluted in DMEM before being applied to the tumor spheroids, but here an equal dilution factor was used for all samples.

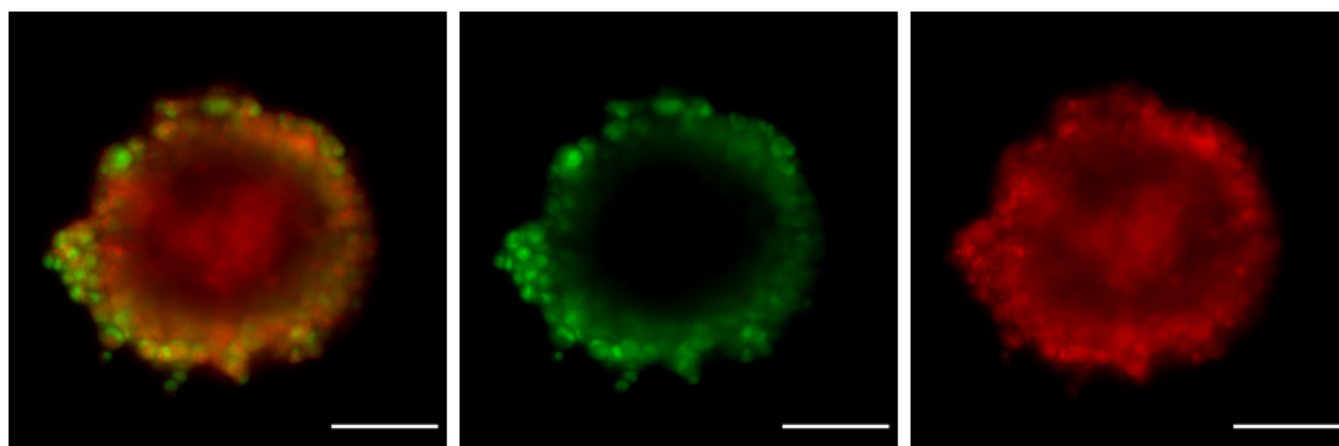


Fig. S3 Optical cross-sections of a spheroid, all at the same depth of 100-140 μm . The representative pseudo-colored images used for quantitative analysis of fluorescence intensity versus penetration depth, d , show the two fluorescence channels; nuclear stain (green) and nanoparticles (red), and their overlay. Scale bars corresponds to 100 μm .